In-process laser scanning for defect detection in material extrusion additive manufacturing

Aryan Rana and Kazem Fayazbakhsh*

Department of Aerospace Engineering, Toronto Metropolitan University, Toronto, Ontario M5B2K3, Canada

*Corresponding author: kazem@torontomu.ca; Tel: (+1) 416-979-5000 ext. 556414; fax: (+1) 416-979-5056; https://orcid.org/0000-0003-3963-8282

Abstract

Additive manufacturing (AM) and material extrusion processes (MEX) have transformed the fabrication of complex parts from a wide range of materials. However, the widespread use of MEX processes is still hindered by the presence of defects induced during 3D printing. This necessitates the development of an in-process defect detection system for MEX techniques. In this study, an integrated 3D printing and laser scanning apparatus is developed to build and inspect parts automatically, and its effectiveness is assessed using specimens designed with intentional gaps. After printing, the apparatus scans each layer, allowing for detailed internal defect detection. Four sets of tensile samples per ASTM D638-22 with varying gap widths along their centerline are explored. Samples consist of 24 layers and feature a gap on their tenth layer with 0° raster orientation. Three samples are 3D printed and scanned for each specimen set using the apparatus (a total of 12). The data sets from the laser scanning are analyzed, the gap widths are obtained, and compared with the expected values from the design corrected for shrinkage. The coefficient of variation for gap width is between 0.23% and 2.5% for all specimen sets, and the magnitude of percent error for all 12 samples is between 0.3% and 3.3%. This validates the repeatability and accuracy of the apparatus in capturing defects and evaluating variability inherent in the layer-based MEX processes. To demonstrate the apparatus's capabilities, a complex part is designed, 3D printed, laser scanned, and reconstructed.

Keywords: Material extrusion processes; Additive manufacturing; Laser scanning; In-process monitoring; Defect detection; Point cloud analysis

The International Journal of Advanced Manufacturing Technology

https://doi.org/10.1007/s00170-025-16145-y

1. Introduction

Additive Manufacturing (AM) has made breakthroughs in the aerospace, automotive, and healthcare industries, and continues to advance manufacturing processes daily. Material extrusion processes (MEX) can manufacture complex parts from a wide range of feedstock. MEX of polymeric and composite filaments, also known as Fused Filament Fabrication (FFF), has widespread applications. High-quality filaments, accurate machines, and optimum manufacturing process parameters can increase the repeatability of the fabrication technique. However, there will always be deviations between as-designed and as-manufactured parts, including defects. Common defects include layer misalignments, stringing, warping, under-extrusions, over-extrusions, and voids [1, 2]. They have a detrimental impact on dimensional accuracy [3] and structural integrity of final parts [4]. While these defects cannot be avoided entirely, a quality control system that can automatically and precisely capture their shape, size, and location is the first step in adopting AM in stringent applications.

Traditional methods of locating defects involve non-destructive and destructive testing techniques, such as ultrasonic imaging [5], thermography [6], computed tomography scanning [7], and optical microscopy [8]. These methods are often utilized post-print; therefore, any defects emerging during the 3D printing process will not be captured until print completion. As a result, some severe defects that might be deemed unacceptable can only be found at the end. This leads to scrap costs, which could have been mitigated if the print was canceled or corrected during fabrication. Furthermore, a post-print inspection means that the accuracy of these techniques is lower for embedded defects than surface-level ones. On the other hand, an in-process fault detection system can locate defects during 3D printing before the deposition of subsequent layers hides them.

Researchers have primarily used optical imaging and computer vision systems for in-process defect detection systems during MEX. Recently, many studies have coupled these systems with machine learning algorithms to categorize images of 3D-printed parts and identify defects. This approach has proven successful in capturing the stringing [9, 10] and warping [11] defects in desktop MEX machines using a camera. While this technique has been used for under-extrusions and over-extrusions [12, 13], they are more challenging to identify since camera angles, part locations, and lighting significantly impact the results. Using a laser profiler to create a point cloud of a 3D printed part that can be compared with the original 3D model can address the limitations of the optical imaging systems. This comparison allows deviations between as-designed and as-manufactured models to be obtained during 3D printing and used as an in-process monitoring technique.

A few studies have explored the use of a laser profiler to capture defects during MEX processes [1]. Xue et al. [14] used a Hyrel 3D printer from System 30M and a Keyence LJ-V7000 series scanner to detect warpage while fabricating a square plate. By using measurements along the z-axis, this study was able to detect and quantify the warpage percentage. Tootooni et al. [15]

utilized a MakerBot 2X 3D printer to fabricate a test piece that they designed, called circle-square-diamond. After fabrication, they used a NextEngine HD laser scanner to get a point cloud of the sample and evaluate deviations from the CAD model. They could use only about 5% of the point cloud to categorize AM parts based on the severity of their dimensional variations.

Identifying under-extrusions and over-extrusions in 3D printed parts using a laser profiler has been investigated by a few researchers. Lishchenko et al. [16] used a Creality Ender-3 3D printer and fabricated rectangular samples with random under-extrusions, stringing, and high roughness. After 3D printing, they scanned the top surface of the part using a Keyence LJ-8020 laser profiler. They could differentiate between defective samples and the baseline; however, this did not include finding defects' shape, size, and location. Furthermore, since they did not design a test case with intentional defects, they used a roughness tester as a validation tool for the laser profiler. Lafirenza et al. [17] also did not have a part with intentional defects, and changed the print location on the build platform and raster angles to induce random defects. They used a GeeeTech A10 3D printer and had a scanControl 2900-50 BL laser profiler fixed on a frame beside it. After each layer completion, the build platform moved it for scanning. The height deviation compared with the CAD model was used to evaluate the surface quality of samples, including under-extrusions. They used a structured light scanner to validate the results from the laser profiler. Moretti et al. [18] used a similar setup with a custom-built 3D printer and a fixed laser source (80 mW at 520 nm). They selected two trapezoidal prisms with internal reticular infills, including features challenging to 3D print, thereby inducing defects during fabrication. For each layer, the binary image from the laser scanner was compared with that from the layer 3D printing simulation. This way, locations with overfill and underfill were identified.

Zheng et al. [19] designed multiple test samples with intentional defects and fabricated them using a custom-built 3D printer. They placed a Keyence LJ-X8060 on a robotic arm and used it for scanning after each layer was completed. They captured defects along the z-axis using height values from the point clouds and classified different types of under-extrusions, namely gaps, holes, and pits. The shape, size, and location of defects were not compared quantitatively with the CAD models. Lin et al. [20] provided a schematic of a scanControl 2600-50 integrated with a multi-material 3D printer. They had a "Baymax" character model and put a small cuboid groove underfill and a cylindrical overfill as intentional defects. Each layer's point cloud was preprocessed and represented by a depth image. By comparing it with the reference depth image from the CAD model, they could capture the defects and later reconstruct 3D models of the defects.

In summary, previous research studies either lacked a fully integrated 3D printing and in-process laser scanning apparatus or did not quantitatively validate repeatability and accuracy of their systems. They did not utilize standardized test samples; therefore, it is challenging to use their results for comparison across multiple studies. Furthermore, since only one specimen per set was fabricated and inspected, they were unable to capture variability inherent in the layer-based MEX processes. This study integrated a laser profiler with a custom-built 3D printer without limiting the scanner's view. The apparatus provides a fully automated process for fabrication and in-process defect detection. Tensile specimens per ASTM D638-22 [21] with intentional gaps were designed as test articles. Each of the four test articles were 3D printed three times to explore variations and random errors between production runs. Furthermore, gap width values were compared with previously obtained results from phased array ultrasonic testing. This way, the accuracy of the defect detection system can be evaluated systematically, and the impact of defects on the tensile properties can be obtained afterward.

In this study, in-process laser scanning for defect detection is developed. Section two describes the specifications of the 2D laser profiler, the design of the modified CR-10 3D printer, and the development of data algorithms. Section three details the results obtained in this work, highlighting the defect detection mechanism and providing a comparative analysis of the results with ultrasonic testing. Furthermore, a complex 3D part was designed, 3D printed, and laser scanned, and its as-manufactured 3D model was reconstructed. The last section concludes the paper, summarizes the key findings, and recommends potential directions for future work to further enhance the in-process defect detection capabilities for MEX processes.

2. Materials and Methodology

2.1. 3D Printing and Scanning Apparatus

This section details the materials and methodology pertinent to investigating an automatic in-process defect detection system for 3D MEX processes. A CR-10 3D printer (Creality, Shenzhen, China), which is a 3-axis cartesian machine, was selected. Motion on the x-axis (the extruder position) and y-axis (the build platform position) is belt and motor driven, while z-axis motion is lead screw and motor driven. The CR-10 3D printer was modified to achieve full closed-loop linear motion using sensors and feedback loops. It should be noted that each axis is driven by its own closed-loop DC servo motor, which was calibrated to support and respond to a much larger mass on the x-axis resulting from the addition of a laser scanner.

A secondary rail, like the extruder assembly, was introduced to the machine to handle the implementation of a laser profiler. This rail is parallel to the extruder assembly and is driven by the same motors; therefore, the extruder and laser scanner move in tandem along the axes. Both are positioned along the same x and z coordinates; however, the laser scanner is offset along the y-axis, positioned to the left of the extruder. Figure 1a depicts the 3D schematic of the apparatus, and Figure 1b shows the final assembly, including the LJ-V7080 laser profiler (Keyence, Osaka, Japan). The 3D printer and the laser profiler are integrated into one system through a computer that communicates with their controllers (Figure 1c). The LJ-V7080 laser profiler utilizes a blue-light laser with a wavelength of 405 nm, which can also be used for scanning transparent and natural color parts. Figure 1d was taken during laser scanning after completing the tenth layer of a 24-layer sample. The laser line can be observed across the width of the sample, which has an intentional gap along the centerline. The laser line is 32 mm wide, while the sample is 19 mm at its widest. Therefore, the laser line also captures parts of the build platform, the skirt, and the stringing. Figure 1e shows a single profile where regions of the build platform, the skirt, the sample, and the gap can be identified based on their z-height. The laser cannot reflect properly from the sample's straight edges, causing missing data points between the build platform and the sample's sides. Note that the gap in the center of the sample is of interest in this study. For the analysis, the acquired scan data will be processed, and the gap will be isolated.

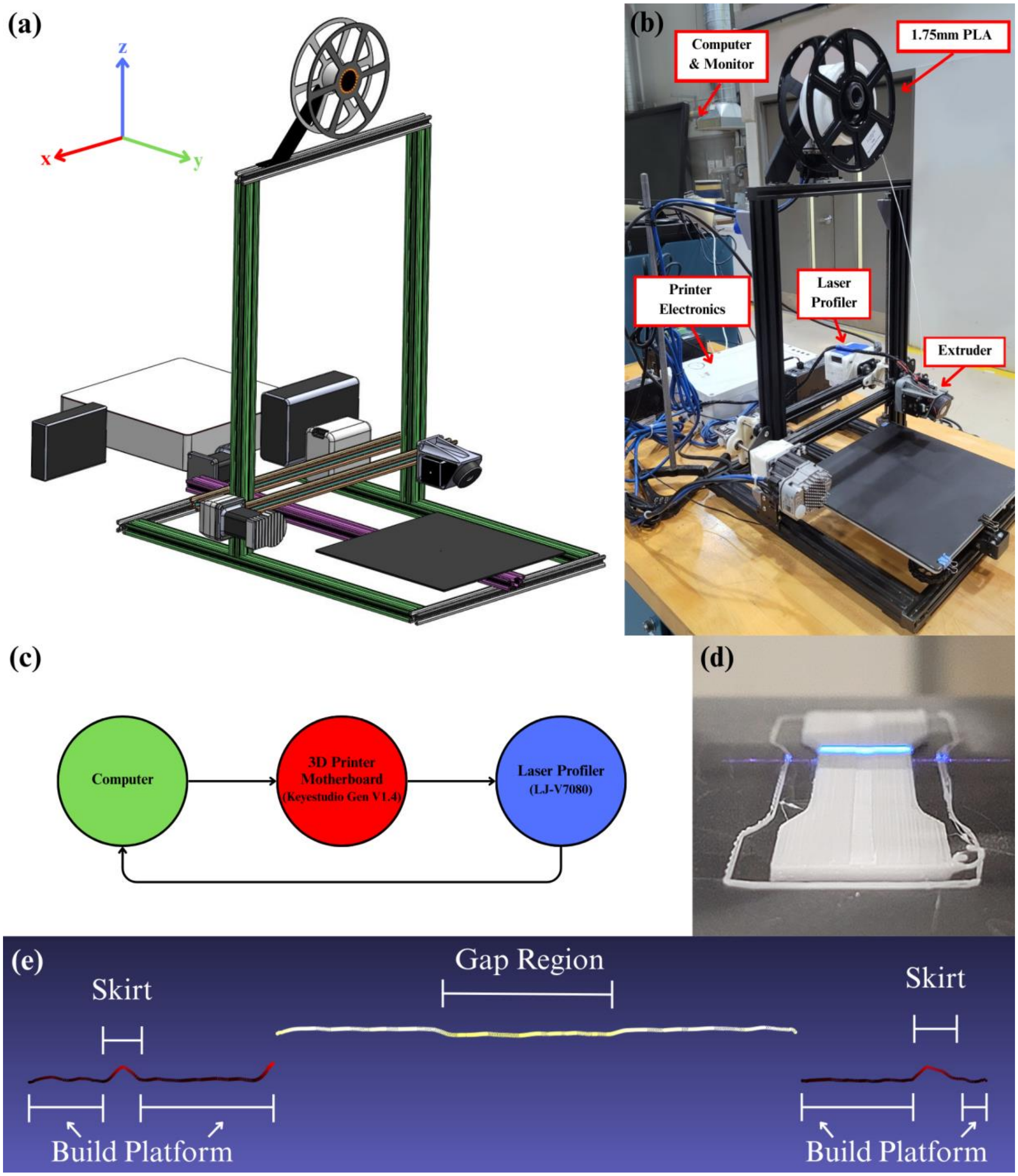

Figure 1. Integrated 3D printing and laser scanning apparatus: (a) schematic of the apparatus; (b) the final assembly including hardware and electronics; (c) the integration process; (d) laser

scanning a sample with an intentional gap along its centerline; and (e) laser profile identifying parts of the build platform, the skirt, the sample, and the gap.

Python was used to integrate laser profiler scanning with 3D printing, allowing for defect detection. First, the script reads the input G-code file and locates the end of each printed layer. Then, scanning path commands are inserted at these locations, allowing the laser profiler to sweep across the printed layer. This process generates an output G-code file and is used in subsequent processes. Note that the scanner and extruder move in tandem; therefore, commands for moving the extruder are used here. Modifying the G-code file allows the laser profiler to be moved across the build platform; however, the code does not handle scanner triggering and data storing. The G-code moves the laser scanner in increments of 0.5 mm. Every time the scanner is moved, the Python script triggers the scanner to capture the profile data. This process is repeated across the build platform. For this increment, the scanning speed was 15 cm/min. For larger parts, larger increments can be used to increase the scanning speed. Furthermore, reducing the time delays from triggering the scanner can increase the printing speed without compromising the resolution.

The scanner has a laser line with a width of 32 mm oriented across the printed layer and stores 800 data points within a single profile in a CSV file. As the laser line moves along the printed layer, profile data is stored in subsequent rows of the CSV file. The accumulation of profiles turns this laser profiler into a quasi-3D-scanner. This data is then processed and analyzed for defect detection, which will be discussed further in Section 2.3. In this study, we are focused on in-process control, which means each layer is scanned after 3D printing. Therefore, defects can be located once a layer is completed and subsequently scanned. While reducing the scanning time is important to decrease the overall time to fabricate and inspect a part, it does not affect the control of the additive manufacturing process. The 3D printing can be stopped after the completion of any layer based on feedback from the inspection system. Furthermore, this in-process inspection method can be scaled to industrial 3D printers since—similar to this study—the laser profiler can be added as a second "extruder" to any gantry-based 3D printer. If the laser line width is smaller than the width of the part, multiple passes are required to scan the entire surface and stitching of point clouds becomes necessary.

A summary of the printing and scanning process can be seen in the flowchart depicted in Figure 2. Note that for n = 0, the laser profiler scans the build platform before sample 3D printing for tilt correction. Prior to this process, the printer deposits a short extrudate outside of the scanning region to prime the nozzle.

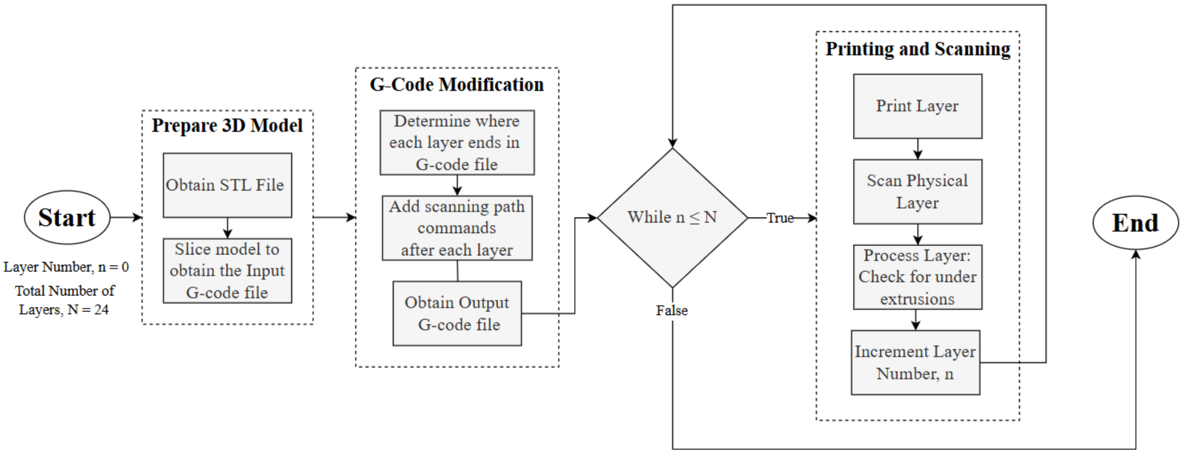

Figure 2. Printing and scanning flowchart.

2.2. Specimen design and manufacturing

A key element of this study is the use of standardized tensile testing specimens per ASTM D638-22. Through standardization, results from different studies can be compared, and 3D printed parts can be used for further research into defects, e.g., their impact on tensile properties. Here, Type I specimen with a specimen thickness of 3.36 mm is utilized (Figure 3). The feedstock was a 1.75 mm white PLA filament, and an extruder temperature of 205 °C and a build platform temperature of 60 °C were used. The layer height was 0.14 mm, which results in a total of 24 layers for the 3D printed sample. The printing speed and infill percentage were 1200 mm/min and 100%, respectively. The stacking sequence is $[45/0/90/-45]_{3s}$, which describes the raster angle of each layer in the model. The angles within the bracket are repeated 3 times, and then are mirrored, as indicated by the subscript 's', which stands for symmetry. Thus, the expanded stacking sequence is [45/0/90/-45 45/0/90/-45 45/0/90/-45 -45/90/0/45 -45/90/0/45 -45/90/0/45].

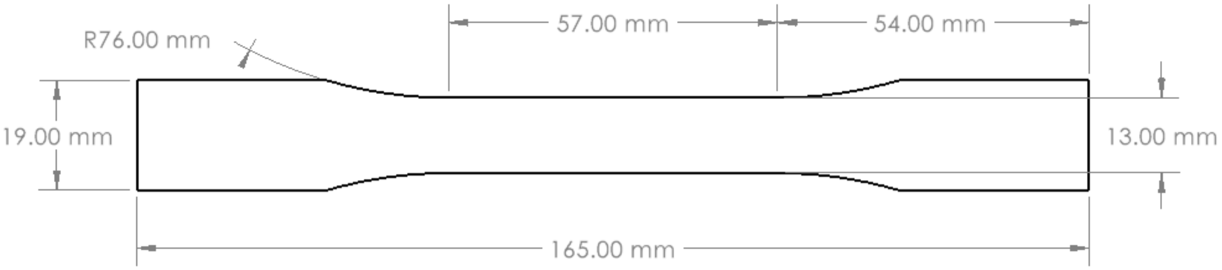

Figure 3. Specimen dimensions.

A total of five specimens were designed, one of which acts as the baseline with no defect while the other four have intentionally embedded defects. All defects occur on the tenth layer, with a 0° raster. This layer has a gap with varying widths along the centerline. This gap progressively enlarges across specimens by increasing the number of missing beads during the 3D printing process. The baseline specimen is a quasi-isotropic specimen with no designed defects. Specimen AA is similar to the baseline, except it has an intentional gap with five beads missing. Each subsequent specimen includes a gap that is two bead widths larger than the preceding one, from AA to AD, with 11 beads missing. Table 1 summarizes the design of specimens in this study. Visualization of the G-Codes for the baseline, AA, and AD specimens using the Prusa G-Code Viewer (version 2.8.0) can be seen in Figure 4. Three samples for each defective specimen set were 3D printed (a total of 12), while the baseline specimen was printed once as a reference.

Table 1. Specimen design summary.

Specimen Set	Defect
Baseline	NO
AA	5 beads missing
AB	7 beads missing
AC	9 beads missing
AD	11 beads missing

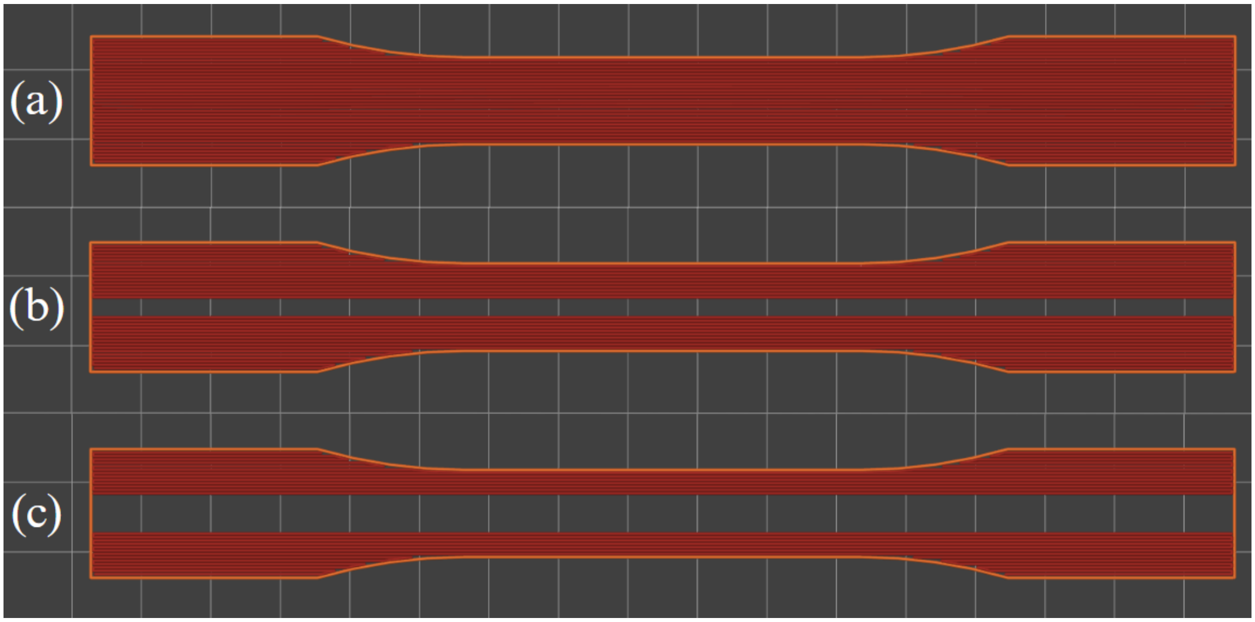

Figure 4. G-Code visualization of tenth layer of samples: (a) baseline; (b) AA with 5 beads missing; and (c) AD with 11 beads missing.

LJ-V7080 laser profiler has a linearity of ±0.046 mm along the z-axis. In other words, it can capture any change in height of more than 0.092 mm. Therefore, this setup can be used confidently to evaluate gaps or overlaps when printing with a layer height of more than 0.092 mm.

In this study, the layer thickness is 0.14 mm, and the gap is included in the sample when 3D printing the tenth layer. Therefore, the height of the sample during scanning is about 1.4 mm. A change in the layer height of about 0.14 mm is an indication of a gap. To validate the apparatus, two thickness gages of 2 mm and 3 mm (Starrett, Athol, USA) were used. Their thickness was measured using a 3732XFL-1 digital micrometer (Starrett, Athol, USA) and was compared with readings from the set-up. A total of 30 measurements were made for each gage using the micrometer, and average thickness values of 1.999 mm and 2.993 mm were obtained. Each gage was placed in three different locations of the build platform and was scanned. The 3D point clouds were used to measure the thickness for each gage, which showed a maximum magnitude of 0.036 mm in variation compared to the actual thickness values. This validates the linearity provided by the manufacturer of the laser profiler and confirms the suitability of the integrated set-up for capturing gaps in this study. All the files for gage thickness testing are included in the data repository.

2.3. Data Preprocessing

Prior to defect analysis, the obtained data must be preprocessed to limit the analysis area to the 3D printed sample. The unfiltered data set contains the build platform and skirt in addition to the 3D printed sample. Therefore, various steps must be taken to filter these data points out of the final data set. These filtering techniques are applied to every layer after scanning. The first step in preprocessing involves the separation of the build platform and sample data. This can be achieved by utilizing a z-axis threshold filtering method. As there is an expected distance between the plane where the platform data points exist and the plane of the 3D printed layer, a plane in between them can be used to separate the two subsets of data. If the overall data set coincides with the xy plane, a z-height value can be used to separate the data. However, since there are small misalignments in the apparatus, specifically the mounting rail for the laser scanner, acquired data was slightly tilted. Two algorithms are utilized to correct the tilt found in the data set. The first step is to quantify the normal vector of the largest plane in the data set. The second step is to correct the tilt with respect to the center of the data. For the first step, a RANSAC plane-fitting algorithm is used to find the data's plane equation. RANSAC is an iterative approach to plane-fitting which maximizes the number of inliers that exist on the plane, while minimizing the numbers of outliers. This removes the influence of outliers on the produced plane equation. From this plane equation, the normal vector can be extracted. Next, the rotation matrix that is used to align this normal vector to the xy plane's normal vector must be calculated. Rodrigues' Rotation Formula can be used to find the rotation matrix and correct the tilt. For a plane with a normal vector defined as $\boldsymbol{n}$, to align the plane with the xy plane, the cross product of $\boldsymbol{n}$, and $\boldsymbol{n_z}$, the normal vector of the xy plane, will provide the axis of rotation: $\boldsymbol{n} \times \boldsymbol{n_z} = \boldsymbol{k} = \left[k_x, k_y, k_z\right]^T$. On the other hand, the angle between $\boldsymbol{n}$ and $\boldsymbol{n_z}$ can be found as: $\theta = \cos^{-1}(\frac{\boldsymbol{n} \cdot \boldsymbol{n_z}}{||\boldsymbol{n}|| \cdot ||\boldsymbol{n_z}||})$. Then, the skew-symmetric matrix is defined as:

$$\boldsymbol{K} = \begin{bmatrix} 0 & -k_z & k_y \\ k_z & 0 & -k_x \\ -k_y & k_x & 0 \end{bmatrix}$$

From here, the skew-symmetric matrix can be utilized to compute the rotation matrix for this transformation: $\boldsymbol{R} = \boldsymbol{I} + (\sin\theta)\boldsymbol{K} + (1 - \cos\theta)\boldsymbol{K}^2$. Then, the normal vector can be rotated: $\boldsymbol{n}_{rot} = \boldsymbol{R}\boldsymbol{n}$. This concept can be extended for a plane composed of a point cloud; for a point cloud P which consists of N points, where each $\boldsymbol{p}_i \in P$, and each point is represented as $\boldsymbol{p}_i = [x_i, y_i, z_i]^T$, each point can be rotated as $\boldsymbol{p}_{i,rot} = \boldsymbol{R}p_i$. Through this process, each point can be rotated using the rotation matrix $\boldsymbol{R}$. Figure 5 depicts layer 0, the build platform, and layer 24 for the baseline specimen before and after the tilt correction. Here, points were assigned colors on a global scale. Colder colors correlate to points further from the scanner, while warmer colors are assigned to points closer to the scanner. The colors from farthest to closest to the laser scanner are black, red, orange, yellow, and white. Figure 5a displays the build platform, and a slight difference in height between the bottom left and top right corners can be observed. This indicates a tilt induced by a tilted build platform and a laser scanner rail. This effect can be seen extended to the 3D printed sample in Figure 5b. After correcting for the tilt, Figure 5c shows the scan data of the build platform with a uniform color across the data. Likewise, Figure 5d displays the correction applied to layer 24.

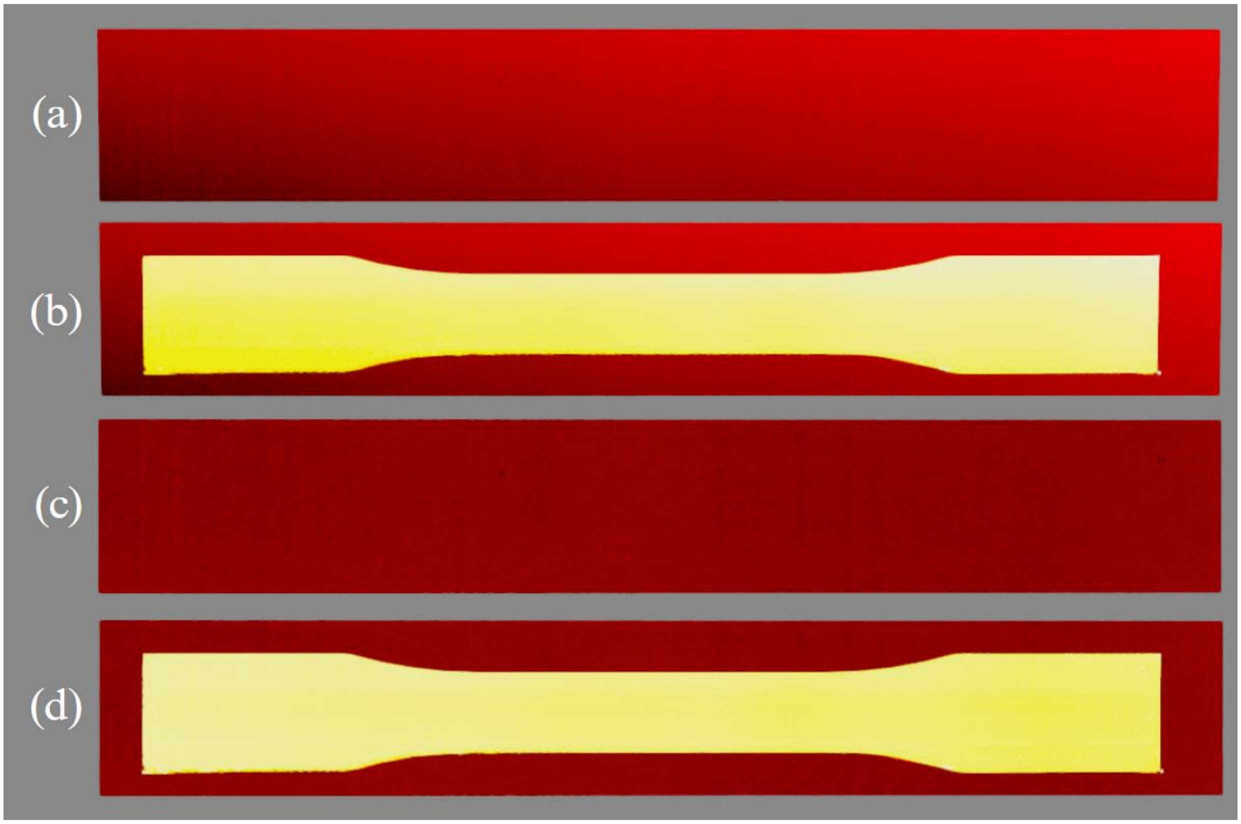

Figure 5. The results of the tilt correction: (a) baseline layer 0 (no correction); (b) baseline layer 24 (no correction); (c) baseline layer 0 (corrected); and (d) baseline layer 24 (corrected)

The next and final step is to crop the point cloud into the shape of the specimen, the region of interest. This can be achieved by using data from the original stereolithography (STL) file of the printed part. The vertices defining each layer can be extracted from this file, and a point-in-polygon test can be conducted to determine which points to include or discard. Here, only a single layer of points was required to be extracted, as the polygon that defines the outer perimeter of the 3D printed part stays the same throughout all layers. An important detail regarding this filtering method is that it must be aligned with the layer data set. One option is to align the polygon points with the printer layer data iteratively; however, any deviations in the scan data (i.e. stringing) may interfere with this alignment and produce incorrect results. Another option is to use the sample's physical location on the build platform and use this data to align the polygon. This was the approach utilized in this study. After alignment, two tests were conducted to separate the point cloud into two groups, i.e., points inside and outside of the polygon. The first test takes the polygon's bounding box and removes any points outside of this region. This test is less intensive than the second test and is used to reduce computational time. The second test utilizes a ray-casting filtering method to remove all remaining points outside of the polygon.

The first test utilizes the polygon's bounding box to remove any points existing outside of the box. For a given polygon $P = \{p_1, p_2, \ldots, p_n\}$, where $p_i = (x_i, y_i)$, the bounding box is defined as the maximum and minimum of the x and y coordinates. Following this, any point $p = (x_p, y_p)$ in the point cloud that does not satisfy the condition: $x_{min} \leq x_p \leq x_{max}$, and $y_{min} \leq y_p \leq y_{max}$, is considered outside of the bounding box and, as a result, outside of the polygon. Figure 6a depicts the specimen's geometry, while Figure 6b shows the bounding box. This test provides an efficient and simple method of reducing the number of points that need to be processed by the more computationally intensive ray-casting filtering that follows.

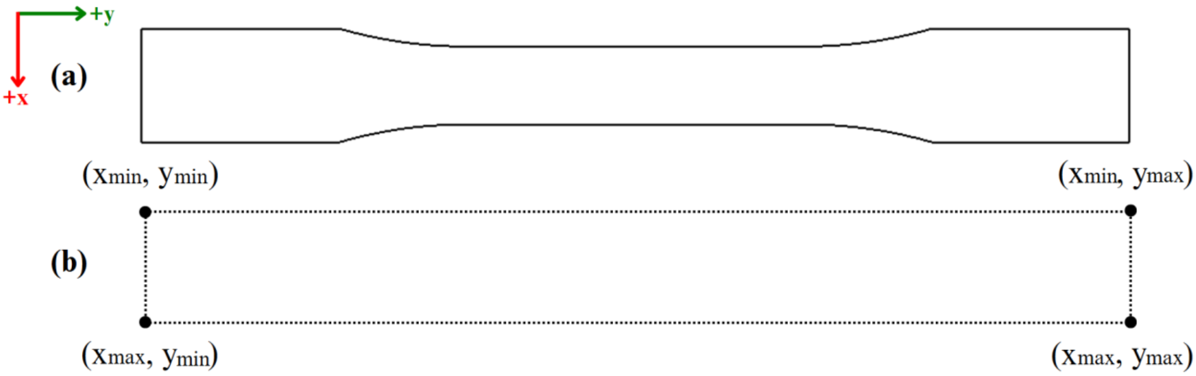

Figure 6. Specimen 2D bounding box.

After filtering out points outside the polygon's bounding box, the ray-casting method is utilized to determine which of the remaining points fit within the polygon. For each point $p = (x_p, y_p)$ in the point cloud, a horizontal ray R_p is cast along the positive x-axis. This ray is defined as $R_p: y = y_p$ for all $x > x_p$. Any intersections with this ray and each of the polygon's edges $e_i =$

$\{(x_i, y_i), (x_{i+1}, y_{i+1})\}$ are noted. The ray intersects an edge at $x_{inter.} = x_i + \frac{(y_p - y_i)(x_{i+1} - x_i)}{y_{i+1} - y_i}$. If $x_p \leq x_{inter.}$, the point lies to the left of the intersection (or on the intersection), and the cast ray must have crossed this edge. The number of intersections for each point $N(p)$ is calculated as the sum of intersections across all polygon edges. If $N(p)$ is an odd number, then that point exists within the polygon, meaning $p \in P$. If $N(p)$ is an even number, then that point exists outside of the polygon, meaning $p \notin P$. Figure 7 provides an example for each case encountered in this filtering process. Notice how the ray corresponding to the red point (on the left side of Figure 7) has an odd intersection number. This indicates that that point exists within the polygon. On the other hand, the ray corresponding to the blue point (at the center of Figure 7) has an even number of intersections, indicating it exists outside of the polygon.

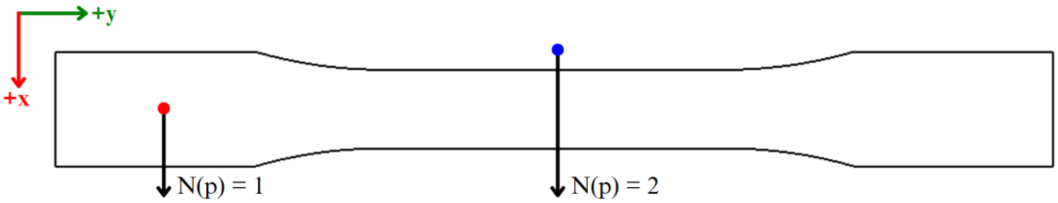

Figure 7. Ray-casting filtering method.

3. Results and Discussions

3.1 Tensile samples

This section examines the results obtained from the 3D printing and laser scanning of the baseline and all three samples of AA to AD specimen sets. It provides comprehensive data analysis and assesses the effectiveness of the methods employed. The discussion also explores the implications of these findings and connects them to the wider context of research in MEX processes.

Figure 8a presents the final layer scan of sample AC1, while Figure 8b is a top-down image of the same sample obtained from a digital camera. The colors seen in the former were assigned based on the global max and min values, i.e., points with a warmer color have a greater z-height. Recall that the colors from farthest to closest to the laser scanner are black, red, orange, yellow, and white. Comparing the results from the laser scanner and the image from the camera, it can be observed that the laser scanner accurately captured the 3D printed sample, the skirt, the stringing, and the blobs. Note that the white color PLA against the black build platform created sufficient contrast for the digital camera to capture details of the 3D printed part. The laser scanner acquired z-height data from the sample and is not dependent on color or lighting.

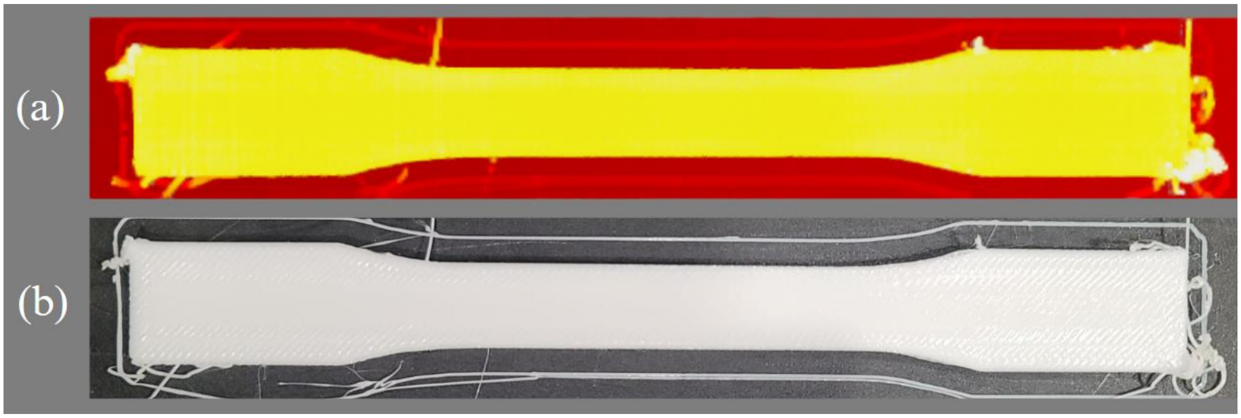

Figure 8. Different representations of sample AC1: (a) z-height color map from the laser scanner; and (b) image from a digital camera.

Figure 9a presents the tenth layer scan of the baseline sample while Figures 9b to 9e present the tenth layer scans of sample AA1, AB1, AC1, and AD1, respectively. Comparing the defective samples with the baseline, the gap along the centerline can be clearly observed. The gap region is distinguishable from the rest of the printed layer by its darker color, indicating that it is further from the scanner than the rest. The gap region is an area of missing beads; therefore, when the tenth layer is completed, the gap region has only nine layers. The gap width progressively enlarges from sample AA1 to AD1, which aligns with the specimen design plan. Note that these samples are presented with a local color scale, meaning that colors are assigned based on the layer maximum and minimum values. At first glance, Figure 9c appears to be drastically different from the other defective samples. Looking at the bottom right corner of Figure 9c, a few points are significantly higher than the rest. These points belong to stringing that occurred near corner of that sample and was attached to it. The presence of stringing in this laser scan has caused the color map to be stretched, causing the majority of data to appear predominantly red due to the relative scaling of the color map.

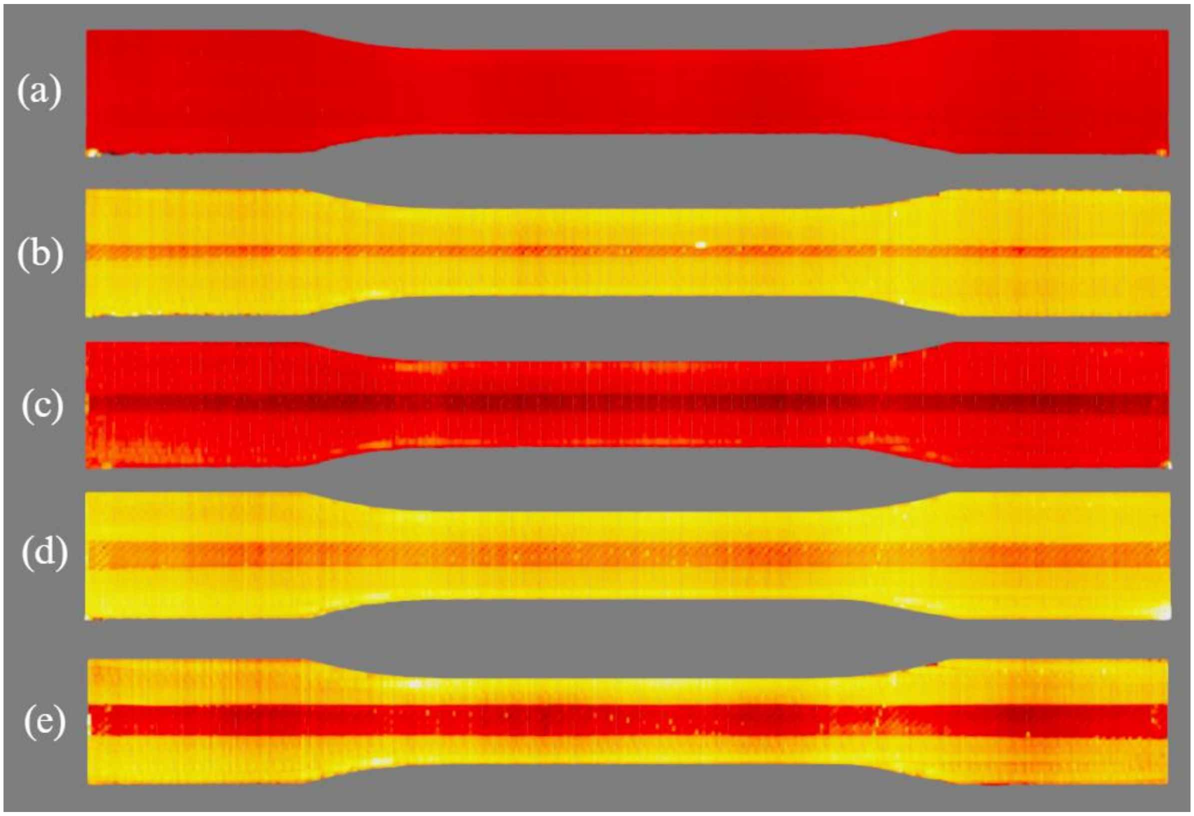

Figure 9. Tenth layer scan comparisons: (a) baseline; (b) AA1; (c) AB3; (d) AC3; and (e) AD1 samples.

Obtaining the gap width of the defective region can be achieved by first isolating the points belonging to the gap, and then measuring the width of the isolated region. Since the defective region is below the expected layer height, it can be isolated using a simple z-threshold filtering process. For each sample, the width of the isolated region at all the points along the sample length is calculated, and the average value is used as the sample gap width.

The gap width in the 3D printed defective samples can be compared with the values from the design (the G-code) with missing beads. However, a correction should be made to account for the sample shrinkage during 3D printing from PLA. The shrinkage percentage can be established by collecting measurements on the 3D printed samples. From Figure 3, the gage and grip widths are designed to be 13 mm and 19 mm, respectively. Using a caliper and collecting five measurements per region and sample, it was found that, on average, all samples were 0.552% smaller than designed. As the laser profiler will be detecting samples that are slightly smaller than expected, it is important to correct the designed gap widths with shrinkage in mind, i.e., the expected gap widths. Table 2 lists the designed gap widths, along with the expected gap widths, which are adjusted for shrinkage. Note that the designed gap width corresponds to five, seven, nine, and 11 beads missing and are obtained from the G-code.

Table 2. Gap widths summary.

Specimen Set	Designed Gap Width (mm)	Expected Gap Width (mm)
AA	2.471	2.46
AB	3.387	3.37
AC	4.333	4.31
AD	5.308	5.28

Now that the expected gap widths are calculated, they can be used to compare with the results from the laser scanner. Table 3 provides the gap width for each defective sample obtained from the laser line scanner. The values are accurate to 0.01 mm, which is the repeatability of the laser profiler along the width. These results align with the intended design plan, with set AA possessing the narrowest gap, followed by set AB, AC, and AD having the widest gap. The coefficient of variation (CV) values listed in Table 3 indicate the variability between different samples of the same specimen set. This value is used to assess the consistency of measurements between prints of the same model. All specimen sets possess a low CV value, with the smallest CV value of 0.23% for specimen set AC, and the largest CV value of 2.5% for specimen set AA. The low CV values across all specimen sets indicate that the 3D printing and the defect detection process have repeatability. Furthermore, the monitoring system successfully captures variations between production runs of the same specimen set.

Table 3. Measured gap widths from the laser scanner.

Specimen ID	Measured Gap Width (mm)	Average (mm)	Coefficient of Variation (%)
AA1	2.44	2.47	2.5
AA2	2.43		
AA3	2.54		
AB1	3.38	3.42	1.4
AB2	3.47		
AB3	3.40		
AC1	4.29	4.28	0.23
AC2	4.28		
AC3	4.27		
AD1	5.14	5.15	0.45
AD2	5.14		
AD3	5.18		

Table 4 compares the measured gap width from the laser scanning apparatus in each defective sample and the expected gap width from the designed model. Note that all specimen sets, barring AB set and sample AA3, possess a percent error slightly in the negatives. Considering the magnitude of percent error, it can be noted that all measurements remain under 4%, confirming the accuracy and repeatability of the results from the laser scanner.

Table 4. Measured and expected gap width values for defective samples.

Specimen ID	Measured Gap Width	Expected Gap Width	Percent Error (%)
AA1	2.44	2.46	-0.81
AA2	2.43		-1.2
AA3	2.54		3.3
AB1	3.38	3.37	0.30
AB2	3.47		3.0
AB3	3.40		0.89
AC1	4.29	4.31	-0.46
AC2	4.28		-0.70
AC3	4.27		-0.93
AD1	5.14	5.28	-2.7
AD2	5.14		-2.7
AD3	5.18		-1.9

Per Table 4, samples AB1 and AA3 possess the largest and smallest percent error, respectively. The varying percent errors between samples and specimen sets may be a function of the variability induced in the 3D printing process. Variations in the filament diameter, machine errors, and obstruction of view impact the as-manufactured defective samples and their gap width measurements compared to the as-designed samples. For example, for sample AA1, an unintended deposition of hot PLA was laid on the gap region during 3D printing. The presence of this unintended defect obstructs the view of the gap, thereby preventing the laser scanner from obtaining data below the deposition (Figure 10a). This results in the computed average width being lower than other points along the sample. Additionally, stringing caused by the nozzle as it passes over the part may result in more deposition of unwanted material. An example of these unwanted depositions for sample AD1 can be seen in Figure 10b. In addition, the laser profiler has a data interval of 0.05 mm; if a laser point does not reflect properly while scanning the gap and its edges, the width measurement will be an underestimation by about 0.05 mm. Surface parameters affect the data quality obtained from the laser profiler. Compared to a red-light laser, the LJ-V7080 profiler uses a blue-light laser with a wavelength of 405 nm, which can better scan transparent and natural color parts. However, surface parameters such as part material and color still influence data quality. Furthermore, certain part geometries may obstruct the reflected laser light, preventing it from reaching the profiler. This can result in missing data points in the readings, or the scanner may interpolate measurement values based on the available data in those regions.

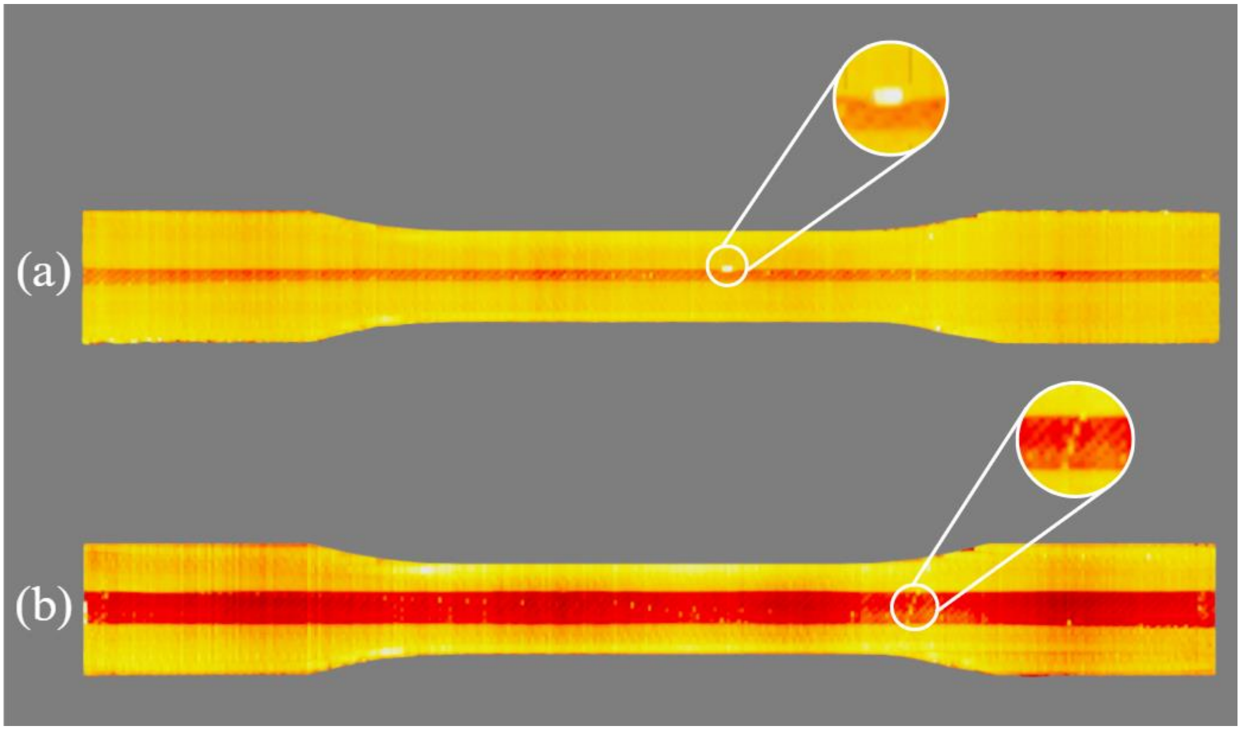

Figure 10. Unwanted material deposition covering regions of the gap: (a) sample AA1; and (b) sample AD1 with some stringing.

In 2021, in a collaborative effort, our research group published a study on detecting gaps in FFF 3D printed samples using phased array ultrasonic testing [22]. The study utilized the same ASTM D638 Type I specimens with intentional gaps with five, seven, nine, and 11 missing beads. However, a Prusa i3 Mk2S (Prusa Research, Prague, Czech Republic) was used to print five samples for each set from a gray PLA filament with a diameter of 1.75 mm. High frequency phased array ultrasonic testing (PAUT) was conducted post-print on all samples, the gap widths were measured, and an average value for each specimen set was obtained. Table 5 compares the gap width from the laser scanner and the PAUT with the expected value for all specimen sets. The highest magnitude of percent error for the laser scanner is only 2.4%, while it is 9.5% for the PAUT. This further validates the accuracy of the proposed in-process 3D printing monitoring and defect detection system.

Table 5. Comparative Analysis between Laser Scanning and PAUT Inspection.

Specimen set	Expected gap width (mm)	Gap width from laser scanner (mm)	Gaps width from PAUT (mm)	Error, laser scanner (%)	Error, PAUT (%)
5 missing beads	2.46	2.47	2.25	0.41	-8.5
7 missing beads	3.37	3.42	3.05	1.4	-9.5
9 missing beads	4.31	4.28	4.50	-0.70	4.4
11 missing beads	5.28	5.15	5.04	-2.4	-4.5

3.2 Complex 3D part

The simple geometry of standardized tensile specimens was needed to systematically evaluate the embedded gaps. However, the apparatus can be utilized to 3D print, laser scan, and construct 3D models of as-manufactured parts with complex geometries. Figure 11a shows the 3D model of a detailed component, and Figure 11b is an image of the part post-print. A stringing defect can be observed in the bottom right hexagonal cell. After processing the laser profile data, a point cloud with all scanned layers of the complex part was produced (Figure 11c), in which the surface of the stringing defect was captured as well. The alpha shape method was used for surface construction from the obtained point cloud, and each consecutive pair of layers was utilized to make a mesh. These meshes were obtained through the built-in alpha shape function in the Python Open3D module and were stacked upon one another for visualization (Figure 11d).

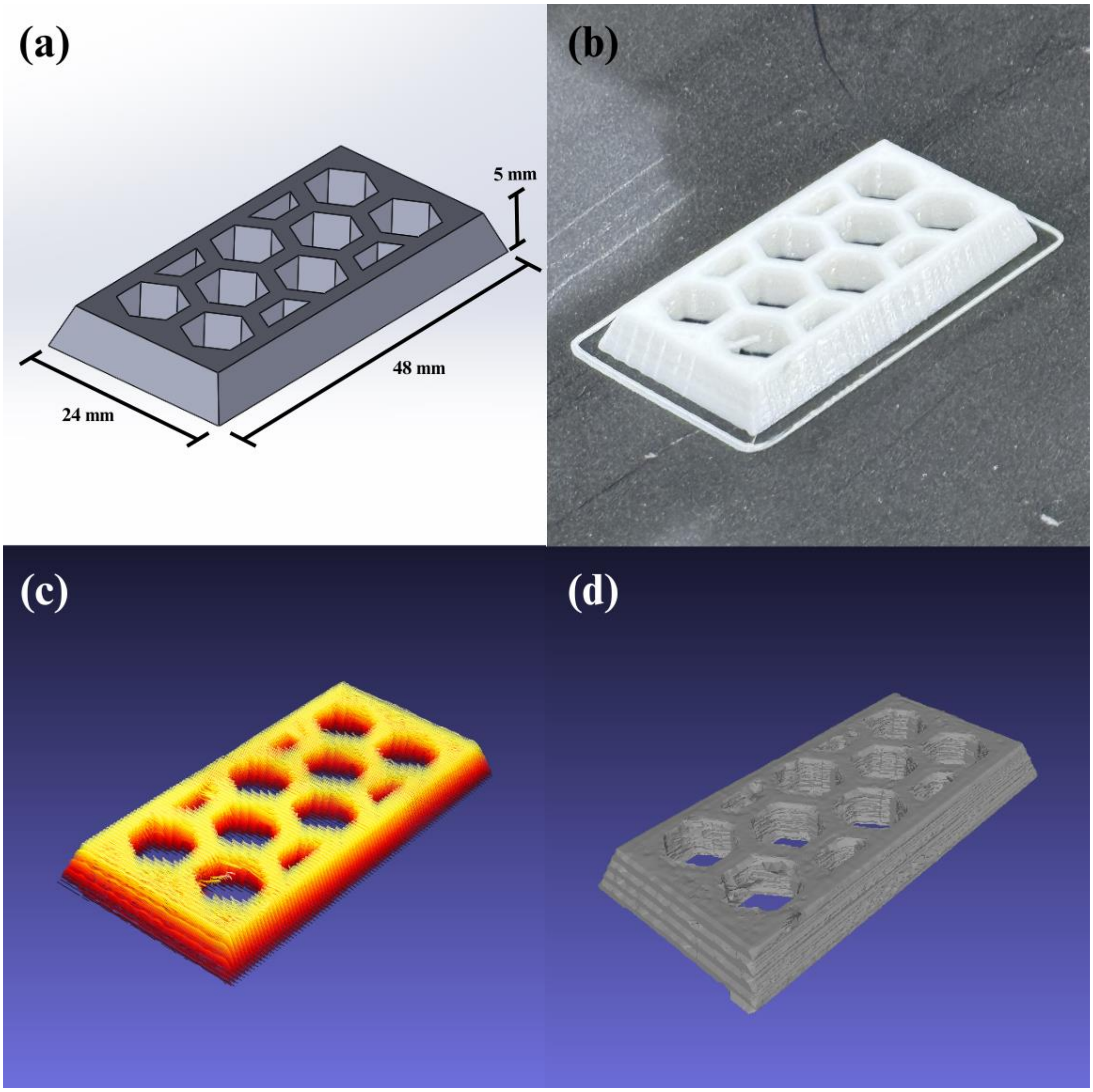

Figure 11. 3D printing, laser scanning, and constructing the 3D model of the as-manufactured part: (a) 3D CAD model; (b) optical image of the 3D printed part; (c) color map of the point cloud from the scanner; and (d) constructed 3D model.

4. Conclusions

This study proposed an in-process laser inspection system for defect detection of 3D printed parts. A Creality CR-10 3D printer was modified to incorporate a laser profiler, the Keyence LJ-V7080, which was swept across the build platform to form a 3D point cloud of the manufactured sample, allowing for analysis of anomalies and inconsistencies. Tensile samples with intentional gaps along the centerline were designed with five, seven, nine, and 11 beads missing on the tenth printed layer, which had a raster angle of 0°. A baseline model with no defects was printed for reference. Each defective specimen set was 3D printed three times to assess the variability of the 3D printing process and the reliability of the defect detection system. After preprocessing and analyzing the data sets from the laser scanner, the gap width for all samples (a total of 12) was measured. The key findings include the following:

- The coefficient of variation for gap width ranged from 0.23% for specimen set AC to 2.5% for specimen set AA.
- The magnitude of percent error between the measured gap width and the expected as-designed value corrected for shrinkage ranged from 0.3% to 3.3%.
- These results validated the repeatability of the laser scanning measurements and demonstrated the capability of the in-process inspection system in evaluating variability inherent in the layer-based MEX processes.

Therefore, the integrated 3D printing and laser scanning apparatus can effectively manufacture and inspect parts from polymeric filaments. Furthermore, a complex 3D part was designed, 3D printed, laser scanned, and reconstructed to demonstrate the apparatus's capabilities.

This experimental procedure effectively examined and detected gaps of varying widths, stringing, and blobs by the developed apparatus. Several other defects are commonly induced during 3D printing processes, e.g., over-extrusions and overlaps. The developed apparatus already possesses the potential to detect such defects; however, the analysis must be developed to accommodate their detection. Future work can aim to add these functionalities. Furthermore, interventions, e.g., pausing the print or corrective actions, can be implemented by receiving feedback from the inspection system. In addition, the apparatus can be improved by reducing the time delays from triggering the scanner, in order to increase the printing speed without compromising the resolution.

Acknowledgments

The author would like to acknowledge the contributions of past researchers at the FRAMES lab, Brent Gebuza, Artin Sarkezians, Levi Gregorash, and Sadben Khan, on the 3D printing and laser scanning apparatus.

Author contribution

Aryan Rana: Conceptualization, Data curation, Formal analysis, Investigation, Methodology, Visualization, Writing – original draft, Writing – review and editing. **Kazem Fayazbakhsh**: Conceptualization, Funding acquisition, Project administration, Resources, Supervision, Writing – review and editing.

Funding

The financial support was provided by the Natural Sciences and Engineering Research Council of Canada (NSERC), RGPIN-2023-04091, and the NSERC Undergraduate Student Research Award.

Data Availability

All information from this study, e.g., G-codes for all specimens, raw data from the laser profiler from all the scans, and processed point clouds, is provided in the data repository (Mendeley Data, V2, doi: https://doi.org/10.17632/vw78jpgpyv.2).

Conflict of interest

The authors declare no competing interests.

References

[1] Selot, A. and Dwivedi, R.K., 2023. Machine learning and sensor-based approach for defect detection in MEX additive manufacturing process-A Review. Journal of the Brazilian Society of Mechanical Sciences and Engineering, 45(10), p.535.

[2] Tao, Y., Kong, F., Li, Z., Zhang, J., Zhao, X., Yin, Q., Xing, D. and Li, P., 2021. A review on voids of 3D printed parts by fused filament fabrication. Journal of Materials Research and Technology, 15, pp.4860-4879.

[3] Côté, R., Demers, V., Demarquette, N.R., Charlon, S. and Soulestin, J., 2023. A strategy to eliminate interbead defects and improve dimensional accuracy in material extrusion 3D printing of highly filled polymer. Additive Manufacturing, 68, p.103509.

[4] Fayazbakhsh, K., Movahedi, M. and Kalman, J., 2019. The impact of defects on tensile properties of 3D printed parts manufactured by fused filament fabrication. Materials Today Communications, 18, pp.140-148.

[5] Lee, K.J., Jeon, M.S. and Lee, J.R., 2023. Evaluation of manufacturing defects in 3D printed carbon fiber reinforced cylindrical composite structure based on laser ultrasonic testing. NDT & E International, 135, p.102802.

[6] Saeed, N., Omar, M.A., Abdulrahman, Y., Salem, S. and Mayyas, A., 2018. IR thermographic analysis of 3D printed CFRP reference samples with back-drilled and embedded defects. Journal of Nondestructive Evaluation, 37, pp.1-8.

[7] Ghorbani, J., Koirala, P., Shen, Y.L. and Tehrani, M., 2022. Eliminating voids and reducing mechanical anisotropy in fused filament fabrication parts by adjusting the filament extrusion rate. Journal of Manufacturing Processes, 80, pp.651-658.

[8] Khosravani, M.R., Božić, Ž., Zolfagharian, A. and Reinicke, T., 2022. Failure analysis of 3D-printed PLA components: Impact of manufacturing defects and thermal ageing. Engineering Failure Analysis, 136, p.106214.

[9] Paraskevoudis, K., Karayannis, P. and Koumoulos, E.P., 2020. Real-time 3D printing remote defect detection (stringing) with computer vision and artificial intelligence. Processes, 8(11), p.1464.

[10] Kim, H., Lee, H., Kim, J.S. and Ahn, S.H., 2020. Image-based failure detection for material extrusion process using a convolutional neural network. The International Journal of Advanced Manufacturing Technology, 111(5), pp.1291-1302.

[11] Saluja, A., Xie, J. and Fayazbakhsh, K., 2020. A closed-loop in-process warping detection system for fused filament fabrication using convolutional neural networks. Journal of Manufacturing Processes, 58, pp.407-415.

[12] Jin, Z., Zhang, Z. and Gu, G.X., 2019. Autonomous in-situ correction of fused deposition modeling printers using computer vision and deep learning. Manufacturing Letters, 22, pp.11-15.

[13] Petsiuk, A.L. and Pearce, J.M., 2020. Open source computer vision-based layer-wise 3D printing analysis. Additive Manufacturing, 36, p.101473.

[14] Xu, K., Lyu, J. and Manoochehri, S., 2022. In situ process monitoring using acoustic emission and laser scanning techniques based on machine learning models. Journal of Manufacturing Processes, 84, pp.357-374.

[15] Samie Tootooni, M., Ashley Dsouza, Ryan Donovan, Prahalad K. Rao, Zhenyu Kong, and Peter Borgesen. "Classifying the dimensional variation in additive manufactured parts from laser-scanned three-dimensional point cloud data using machine learning approaches." Journal of Manufacturing Science and Engineering 139, no. 9 (2017): 091005.

[16] Lishchenko, N., Piteľ, J. and Larshin, V., 2022. Online monitoring of surface quality for diagnostic features in 3D printing. Machines, 10(7), p.541.

[17] Lafirenza, M., Guerra, M.G. and Lavecchia, F., 2023. A layerwise monitoring methodology based on blue laser line profilometer for Material Extrusion processes. The International Journal of Advanced Manufacturing Technology, 127(11-12), pp.5421-5436.

[18] Moretti, M., Rossi, A. and Senin, N., 2024. Optical tomography by laser line scanning and digital twinning for in-process inspection of lattice structures in material extrusion. Additive Manufacturing, 93, p.104424.

[19] Zheng, Q., Zou, B., Chen, W., Wang, X., Quan, T. and Ma, X., 2023. Study on the 3D-printed surface defect detection based on multi-row cyclic scanning method. Measurement, 223, p.113823.

[20] Lin, W., Shen, H., Fu, J. and Wu, S., 2019. Online quality monitoring in material extrusion additive manufacturing processes based on laser scanning technology. Precision Engineering, 60, pp.76-84.

[21] ASTM D638-22, 2022. ASTM International. Standard Test Method for Tensile Properties of Plastics.

[22] Fayazbakhsh, K., Honarvar, F., Amini, H. and Varvani-Farahani, A., 2021. High frequency phased array ultrasonic testing of thermoplastic tensile specimens manufactured by fused filament fabrication with embedded defects. Additive Manufacturing, 47, p.102335.